ASIAN JOURNAL OF PHARMACEUTICAL AND CLINICAL RESEARCH

INNOVARE ACADEMIC SCIENCES
Knowledge to Innovation

Vol 18, Issue 10, 2025

Online - 2455-3891
Print - 0974-2441

Research Article

DEVELOPMENT AND OPTIMIZATION OF NANOCOCHLEATE-BASED DIOSMIN CARRIERS FOR CANCER TREATMENT

SARDAR SHELAKE[1]*, SHITALKUMAR PATIL[2]

[1]Department of Pharmaceutics, Ashokrao Mane College of Pharmacy, Shivaji University, Kolhapur, Maharashtra, India.
[2]Department of Pharmaceutics, Dr. J. J. Magdum College of Pharmacy, Jaysingpur, Maharashtra, India.
*Corresponding author: Sardar Shelake; Email: sardarshelake289@gmail.com

Received: 10 August 2025, Revised and Accepted: 22 September 2025

ABSTRACT

Objectives: This study aimed to develop and optimize diosmin-loaded nanocochleates (NCs) as a potential targeted delivery system for cancer therapy.

Methods: A three-factor, three-level Box-Behnken design was employed to evaluate the effects of phospholipid choline (Factor A), cholesterol (Factor B), and stirring speed (Factor C) on particle size, entrapment efficiency, and polydispersity index. Diagnostic plots confirmed the model's robustness, with normal distribution of residuals and strong correlation between predicted and actual values.

Results: Interaction and 3D surface plots revealed that higher phospholipid and cholesterol concentrations increased particle size and entrapment efficiency, while optimal stirring speed improved uniformity. Fourier-transform infrared spectroscopy confirmed diosmin encapsulation by showing shifts in O–H and C=O stretching peaks, suggesting hydrogen bonding and lipid interactions. Differential scanning calorimetry further supported the drug's successful encapsulation by revealing the disappearance of diosmin's endothermic peak, indicating conversion from crystalline to amorphous form. *In vitro* drug release studies showed sustained release of diosmin from the NCs compared to the pure drug, highlighting enhanced solubility and prolonged availability. Cell cycle analysis using flow cytometry demonstrated that the optimized formulation induced significant cell cycle arrest in MCF-7 breast cancer cells, confirming its potential antiproliferative activity.

Conclusion: These findings validate the NC system as a promising platform for targeted diosmin delivery, offering improved encapsulation efficiency, stability, sustained release, and therapeutic efficacy. The optimized formulation achieved a desirable balance among key parameters, supporting its application in cancer nanomedicine.

Keywords: Cell cycle, Breast cancer, Apoptosis, QbD.

 DOI: http://dx.doi.org/10.22159/ajpcr.2025v18i10.56929. Journal homepage: https://innovareacademics.in/journals/index.php/ajpcr

INTRODUCTION

Breast cancer is the most common type among women, and it continues to be one of the world's top causes of death [1,2]. Globally, breast cancer caused 685,000 deaths and more than 2.3 million new cases in 2020. According to projections, the disease would cause more than 3 million new cases and 1 million deaths yearly by 2040, mostly as a result of aging and population expansion [3].

Current medicines including chemotherapy, radiation, and surgery still face issues such as drug resistance, systemic toxicity, and limited focused efficacy, despite advancements in early detection and treatment [4,5]. Many times, chemotherapy drugs exhibit non-specific toxicity to healthy cells, which can result in serious side effects and a worse standard of living for patients [6]. Therefore, improving the results of cancer treatment requires the development of innovative therapeutic approaches that increase drug efficacy while lowering adverse effects [7]. Citrus fruits are the primary source of diosmin, a flavonoid glycoside that has drawn a lot of interest because of its diverse range of pharmacological actions, which include anti-inflammatory, antidiabetic, anti-cancer, antihyperlipidemic, and antioxidant properties [8,9]. Due to its venotonic qualities, diosmin has been utilized for many years, especially as a vascular protective medication to treat hemorrhoids [10,11]. Diosmin has demonstrated great promise in modifying important molecular processes that contribute to the development of cancer, such as preventing angiogenesis, lowering metastasis, and causing tumor cells to undergo apoptosis [12,13]. By altering important cellular signaling pathways, studies have demonstrated that diosmin can stop the proliferation of several cancer cell lines, including breast cancer cell lines [14-16].

Diosmin's therapeutic potential is severely limited by issues such as poor water solubility, limited bioavailability, and rapid systemic clearance, despite its encouraging anticancer characteristics [17]. When it comes to the formulation and development of bioactive natural chemicals, such as flavonoids like diosmin, poor solubility and restricted bioavailability are significant challenges [18]. The therapeutic efficacy of diosmin is impeded by its pharmacokinetic constraints, which include limited solubility in aqueous media [19]. Due to its limited solubility, it is not as well absorbed in the gastrointestinal tract, which leads to less than ideal plasma concentrations that fall short of the intended therapeutic values [20]. After oral delivery, poor drug breakdown results in low bioavailability and notable inter-subject variability. Reduced solubility impairs drug absorption, making it more susceptible to external factors such as diet and dosage schedules. Therefore, for successful oral administration, a higher standard dose of Diosmin (500 mg twice daily) is usually required. In clinical settings, patients are required to take high dosages for prolonged periods of time, and there is a 12% chance of negative effects, especially gastrointestinal distress [21]. The development of effective drug delivery technologies that improve Diosmin's solubility and bioavailability while also enabling controlled and targeted distribution to malignant tissues is essential to overcoming these obstacles and enhancing treatment results. New drug delivery methods, such as liposomes [22], solid lipid nanoparticles [23], bilayer nanoparticles [24], silver nanoparticles [25], nanostructured lipid carriers [26], nanosuspensions [21], nanosponges [27], and cyclodextrin complex [28], have been studied to overcome the poor dissolution of flavonoids. However, problems like low drug loading capacity, poor drug stability, and the use of excessive excipients that may cause unanticipated safety concerns make it difficult to produce these dosage forms.

Lipid-based nanostructures known as nanocochleates (NCs) are attracting a lot of interest as a cutting-edge medication delivery method [29-31]. These lipid-drug complexes, which are mostly made of phospholipids, have the ability to encapsulate hydrophilic and hydrophobic medications, improving their stability and solubility [32]. Improved bioavailability, longer circulation time, and defense against enzymatic degradation of encapsulated medications are only a few benefits of using NCs. They can interact with cell membranes thanks to their special multilayered structure, which promotes effective medication absorption [33,34]. Furthermore, targeting ligands can be functionalized into NCs to facilitate targeted drug delivery to cancer cells, reducing off-target toxicity and improving therapeutic efficacy [35]. As a result, particularly in anticancer treatment, NCs are showing promise as a remedy for the drawbacks of traditional drug delivery methods. Doxorubicin [36], curcumin [37], and fisetin [38] are just a few of the medications they have successfully delivered, demonstrating their potential to increase effectiveness and lessen adverse effects in the treatment of cancer.

Applying NCs to Diosmin in the treatment of breast cancer is a promising way to get over the drug's drawbacks, given its benefits in improving the bioavailability and targeted delivery of therapeutic compounds. Diosmin's solubility and stability can be greatly increased by encapsulating it in NCs, which will increase its bioavailability. Furthermore, prolonged medication concentrations can be guaranteed by the controlled release characteristics of NCs, which lessens the need for frequent dosage and enhances patient compliance.

A number of factors, such as the lipid composition, drug load, and production circumstances, must be carefully optimized to synthesize diosmin-loaded NCs (D-NC) [39,40]. An efficient statistical technique for pharmaceutical formulation optimization is the Box-Behnken design (BBD), which enables the methodical assessment of several formulation parameters and the determination of the parameters that optimize the therapeutic potential of the drug [41]. To guarantee the optimal formulation, BBD can optimize important parameters such as drug release profiles, encapsulation efficiency, zeta potential, and particle size. The creation of a more effective and repeatable D-NC device for targeted breast cancer treatment will be made possible by this improvement.

To improve the drug's stability, anticancer activity, and bioavailability, this work intends to create and optimize D-NCs utilizing BBD. The method aims to enhance Diosmin's therapeutic results in the treatment of breast cancer by means of strategic formulation and optimization, offering a viable substitute for conventional chemotherapeutic drugs and resolving the difficulties associated with Diosmin's clinical use.

MATERIALS AND METHODS

Materials

A gift sample of diosmin was obtained from Serdia Pharmaceuticals Pvt. Ltd. in Mumbai, India. We purchased cholesterol and phospholipid (phosphatidylcholine) from Lipoid GmbH in Germany. Analytical-grade ethanol, sodium chloride (NaCl), calcium chloride dihydrate ($CaCl_2 \cdot 2H_2O$), and other reagents and solvents used in the investigation were acquired from S.D. Fine Chemicals Ltd. in Mumbai, India. Every chemical was utilized without any additional purification. Water that had been double-distilled was utilized for all experimental methods.

Various instruments/equipment used

The study utilized various laboratory instruments, including a ultraviolet (UV)-Visible Spectrophotometer (Shimadzu UV-1800, Japan), rotary evaporator (Superfit PBU6D), Fourier-transform infrared spectroscopy (FTIR) (Agilent Cary 630 or Bruker Alpha II ATR, Japan), transmission electron microscopy (TEM) (JEOL JEM 2100 plus, Japan), differential scanning calorimeter (Universal V4.5A, TA Instruments), Horiba particle size analyzer (SZ-100, ver. 2.40), freeze dryer (Alpha 1–2 LD plus, Martin Christ), magnetic stirrer (MS 500, Remi Instrument Ltd., Mumbai), digital balance (CAI-234), and distillation unit (Labline LSC-65).

Method: Preparation of diosmin-loaded nanoliposomes

Multi-lamellar vesicle liposomes were created using the thin film hydration method as reported in our earlier study [33]. The lipid phase comprised mixtures of cholesterol and phosphatidylcholine in various molar ratios (Table 1). In brief, the lipid mixture and 50 mg of diosmin were dissolved in a 3:3 v/v chloroform solution, then evaporated under vacuum at 45°C. This resulted in a thin, dry lipid layer on the flask wall, produced using a rotary flash evaporator. The lipid film was hydrated by adding phosphate buffer (pH 7.4) and mixing vigorously with a vortex mixer (Remi, India) at the stirring speed specified in Table 1. This process was continued until all solvent traces were eliminated, allowing vesicle formation to occur. The liposomes were further reduced in size using a sonicator to create small unilamellar vesicles.

Preparation of D-NCs

D-NCs were synthesized through the trapping method. Initially, the diosmin-encapsulated liposomes were subjected to vortex mixing, after

Table 1: BBD design matrix generated for nanocochleates formulation

Std	Run	Factor 1	Factor 2	Factor 3	Response 1	Response 2	Response 3
		A: Conc. of phosphatidyl choline	B: Conc.of Cholesterol	C: Stirring Speed	Particle size	Entrapment efficiency	PDI
		mg	mg	rpm	nm	%	
10	1	600	400	600	211.4	80.41	0.425
5	2	400	300	600	121.6	67.44	0.204
1	3	400	200	700	85.9	77.3	0.634
3	4	400	400	700	145.3	73.39	0.342
12	5	600	400	800	174.2	82.36	0.453
15	6	600	300	700	157.5	81.20	1.206
16	7	600	300	700	157.5	81.20	1.261
17	8	600	300	700	157.5	81.20	1.166
14	9	600	300	700	157.5	81.20	1.246
7	10	400	300	800	103.2	62.27	1.232
4	11	800	400	700	242.4	83.24	0.797
13	12	600	300	700	157.5	81.20	2.266
9	13	600	200	600	192.4	80.17	0.784
2	14	800	200	700	238.1	81.64	0.606
11	15	600	200	800	198.1	80.59	0.696
6	16	800	300	600	226.9	80.97	0.292
8	17	800	300	800	215.0	82.57	0.397

BBD: Box-Behnken design, PDI: polydispersity index

which 50 µL of 0.1 M calcium chloride solution was added gradually in a dropwise manner. The addition of calcium ions triggered turbidity in the liposomal suspension, signifying the successful formation of NCs [37].

Experimental design

A BBD was applied through Design-Expert software Version 13.0 (Stat-Ease Inc., Minneapolis, USA) to evaluate how three variables – phosphatidyl choline concentration (X1), cholesterol concentration (X2), and stirring speed (X3) – influence the formulation characteristics of NCs, specifically particle size (Y1), entrapment efficiency (Y2), and polydispersity index (PDI) (Y3). Factor levels were defined as follows: −1 (400 mg), 0 (600 mg), and +1 (800 mg) for phosphatidyl choline; −1 (200 mg), 0 (300 mg), and +1 (400 mg) for cholesterol; and −1 (600 rpm), 0 (700 rpm), and +1 (800 rpm) for stirring speed. The BBD produced 17 experimental combinations, as detailed in Table 1, to comprehensively cover the experimental space and capture both factor interactions and quadratic effects.

To assess the statistical relevance of the outcomes, an analysis of variance (ANOVA) was conducted. Diagnostic plots, contour plots, and response surface graphs were created to explore the relationships among the variables. Each response variable was analyzed using regression analysis, with models fitted to describe the interactions between factors and responses. Model suitability was confirmed with metrics including R^2, adjusted R^2, predicted R^2, and Adeq Precision, which collectively indicated strong model reliability and predictive accuracy [42].

Formulation optimization

The optimization was conducted using the desirability approach, aiming to maximize entrapment efficiency while minimizing particle size and PDI. Each response was converted to a desirability function ranging from 0 (least desirable) to 1 (most desirable), and an overall composite desirability score was calculated. The optimal formulation, identified with a desirability score close to 1, achieved a balance among particle size, entrapment efficiency, and PDI, demonstrating both the model's robustness and the effectiveness of the desirability approach in optimizing D-NC formulation [43].

Freeze drying of D-NC

The formulation was mixed with 5% w/v trehalose as a cryoprotectant and transferred into vials. The samples were frozen at −40°C, then subjected to freeze drying in a lyophilizer(alpha1-2LD+ Martin christ). Primary drying was conducted at −40°C––50°C and a pressure of 0.01–0.001 mbar to allow sublimation of water. Secondary drying was performed at 20°C–30°C and pressure below 0.001 mbar to remove residual moisture. The freeze-dried solid formulation was sealed under vacuum and stored in a moisture-free environment [44].

Characterization of developed formulation

Particle size

Particle size estimation was conducted using the HORIBA SZ-100 particle size analyzer. Each sample was dispersed in a water at a constant temperature of 25°C to maintain sample stability. The analysis was performed at a scattering angle of 90°, with particle size measurements derived from scattering light intensity data. Results were reported in terms of particle diameter (nm) and frequency (%), providing the mean particle size and standard deviation (SD) [45].

Zeta potential

Zeta potential measurements were performed using the HORIBA SZ-100 particle size analyzer. The sample was prepared in a dispersion medium with a viscosity of 0.897 mPas. During the measurement, the sample holder was maintained at a temperature of 25°C. The system's electrode voltage was set to 3.4 V, and conductivity of the dispersion medium was measured at 0.170 mS/cm. Zeta potential was determined by analyzing the electrophoretic mobility of particles within the medium, providing insights into particle stability and surface charge distribution in the formulation [46].

Entrapment efficiency

The percentage EE of diosmin in D-NC was determined using the methods reported earlier [47,48]. The D-NCs were first collected and dissolved in an appropriate solvent to release the encapsulated diosmin. The actual drug content was then quantified using a UV spectrophotometer at the 270 nm. The theoretical drug content was calculated based on the initial amount of diosmin added during the formulation. The percentage of entrapment efficiency was calculated using the formula:

$$\%EE = \frac{\text{Actual drug content}}{\text{Theoretical drug content}} \times 100 \quad \text{(Eq. 1)}$$

Where the actual drug content was determined experimentally, and the theoretical drug content was based on the amount initially incorporated into the NCs.

TEM analysis

To estimate the morphology and size of the D-NC formulation, TEM was performed. A small drop of the nanoformulation was placed on a carbon-coated copper grid and allowed to dry. The sample was then examined under a TEM (JEOL JEM 2100 plus, Japan) operated at an accelerating voltage of 80 kV. Images of the nanoparticles were captured at various magnifications to analyze their shape, size distribution, and overall morphology. The particle size was measured from the TEM images using appropriate image analysis software [49].

Solid state characterization

FTIR analysis

FTIR spectra of the pure drug, physical mixture, and formulation were recorded using a FTIR (Agilent). Each sample was prepared by mixing 1 mg of the sample with 100 mg of KBr and compressing it into a pellet. Spectra were collected in the 4000–600 cm^{-1} range with a resolution of 4 cm^{-1} and 32 scans. The spectra were analyzed to detect characteristic peaks and assess potential interactions [50,51].

Differential scanning calorimetry (DSC) analysis

DSC analysis of pure drug, physical mixture, and formulation was performed using a SDT Q600 instrument (TA Instruments, V20.9 Build 20). The sample was analyzed under a nitrogen atmosphere with a flow rate of 50 mL/min. The temperature was ramped from 30°C to 350°C at a rate of 10°C/min [52,53].

***In vitro* drug release study**

For the *in vitro* dissolution study using a dialysis membrane, a dialysis bag with a molecular weight cutoff of 12–14 kDa was used. D-NC and pure diosmin were placed inside the dialysis membrane, which was securely sealed. The dialysis bag was immersed in a dissolution medium, phosphate-buffered saline (PBS, pH 7.4), at a constant temperature of 37°C±0.5°C, with continuous stirring at 50 rpm. At predetermined time intervals of 2, 4, 6, 8, 10, 12, and 24 h, 1 mL aliquots were withdrawn from the dissolution medium and replaced with an equal volume of fresh PBS to maintain sink conditions. The withdrawn samples were analyzed spectrophotometrically at 270 nm, and amount of diosmin released was estimated using calibration curve equation y=0.0264×–0.0285 R^2=0.9959 [37,54]. The release profiles of D-NC and pure diosmin were plotted to evaluate the dissolution characteristics.

Cell cycle analysis by flow cytometer

Cell cycle analysis was performed using flow cytometry to assess the effect of the formulations on MCF-7 (Human Breast Cancer) cells. Cells were seeded in 24-well flat-bottom microplates containing sterile coverslips and incubated overnight at 37°C in a CO_2 incubator to allow adherence. The following day, cells were treated with the IC50 concentrations of both pure diosmin 63.16±0.86 µg/mL and D-NC 19.67±0.24 µg/mL for 12 h. Each treatment was carried out in triplicate (n=3).

Post-treatment, cells were washed with 1× PBS and centrifuged at 200×g for 5 min at 4°C. The supernatant was discarded, and the cells

were resuspended in 0.5 mL PBS at a concentration of 1×10^5 cells. Ice-cold 70% ethanol (4.5 mL) was added dropwise for fixation, and samples were incubated on ice for 2 h. After centrifugation (200×g, 5 min, 4°C), ethanol was removed, and the pellet was washed with PBS.

The pellet was then incubated with 1 mL of propidium iodide (PI) staining solution (50 µg/mL PI and 100 µg/mL RNase A in PBS) for 15 min at 37°C in the dark. Flow cytometric analysis was performed within 30 min using a Cytomics FC500 Flow Cytometer (Beckman Coulter, USA). Data were analyzed using FlowJo software to determine the percentage of cells in each phase of the cell cycle (Sub-G1, G0/G1, S, and G2/M). Results are presented as mean±SD. Statistical significance between groups was evaluated using one-way ANOVA followed by Tukey's *post hoc* test, with $p<0.05$ considered statistically significant [55].

RESULTS AND DISCUSSION

Quadratic model was found to be the best fit for each response. Model was found to be significant with F values of 42.30 for Y1, 61.43 for Y2, and 26.31 for Y3. With a mean response of 173.06 and a SD of 9.80, the model's coefficient of variation for Y1 was 5.66%. A good degree of correlation between the predicted and experimental values was indicated by the R^2 value of 0.9769. The model's dependability was confirmed by the reasonable agreement between the adjusted R^2 (0.9538) and predicted R^2 (0.7712), with the difference being <0.2. A robust signal-to-noise ratio was indicated by an adequate precision of 20.213, which is significantly higher than the ideal threshold of 4. These findings suggest that the model for Y1 is adequate for navigating the design space.

With a mean response of 79.31 and a SD of 1.01 for Y2, the model's accuracy is demonstrated by the extremely low C.V.% of 1.27. The model's validity was confirmed by the high R^2 value (0.9875) and adjusted R^2 value (0.9714), as well as the good agreement between the adjusted R2 and the predicted R^2 (0.8000). This model's robustness is further supported by a sufficient precision value of 31.452, which shows an excellent signal-to-noise ratio. As a result, the Y2 model can be used to explore the design space.

With a mean value of 1.07 and a SD of 0.2562, Y3 had a relatively higher C.V.% of 23.94, which would indicate more variability in this response. However, with a difference of <0.2, the R^2 value of 0.9404, adjusted R^2 of 0.9047, and predicted R^2 of 0.7617 were all in reasonable agreement. A good signal-to-noise ratio is shown by the suitable precision value of 11.612. Consequently, the model for Y3 is also regarded as sufficient for navigating the design space, even with the increased variability.

Phosphatidylcholine concentration (A), phosphatidylcholine-cholesterol interaction (AB), quadratic terms of cholesterol (B^2), and stirring speed (C^2) were found to be significant for particle size. The quadratic terms A^2, B^2, and C^2, the interactions AB and AC, and the phosphatidylcholine (A) concentration significantly impacted the entrapment efficiency. Only the quadratic terms A^2, B^2, and C^2 had a substantial impact on the PDI. Results of ANOVA are shown in Table 2.

Effect of variables on formulation characteristics

The normal probability plots (Fig. 1) display the residuals for each response variable in the study. Each plot compares the externally studentized residuals against a theoretical normal distribution. A straight line pattern on these plots generally indicates that the residuals follow a normal distribution, validating the assumption of normality in the model. In all three plots (Fig. 1a-c), the data points closely follow the red diagonal line, indicating that the residuals are normally distributed with no major deviations or outliers. This normality suggests that the models used for predicting the responses are appropriate and that the observed values are consistent with the theoretical expectations.

The residuals versus the run plots (Fig. 1d-f) show the distribution of residuals across the sequence of experimental runs. In Fig. 1d, the residuals are mostly contained within the red control limits, indicating that no significant outliers or patterns are present. Fig. 1e, however, shows two points that slightly exceed the control limits, suggesting the possibility of isolated instances where the model may not perfectly capture the data. Fig. 1f also has one point outside the control limits, but overall, the residuals appear to be randomly distributed. The random pattern in these plots confirms that there is minimal bias due to run order, reinforcing the stability and reliability of the model predictions across different experimental runs. The predicted vs. actual plots assess the accuracy of the model by comparing the predicted values with the actual observed values for each response. Ideally, if the model predictions were accurate, the points would align closely along the diagonal line, indicating that the predicted values are in good agreement with the actual values. In Fig. 1g, the data points lie close to the diagonal line, indicating a high level of agreement between predicted and actual values for particle size. Fig. 1h also shows a strong alignment of data points along the line, with only a few minor deviations, suggesting that the model is reliable. In plot I, the points show some dispersion around the line, especially at lower values, which may indicate a slight deviation in model accuracy for PDI. Overall, strong alignment in these plots demonstrates that the models used are effective in predicting the responses, with only minor discrepancies in some cases.

The interaction plots revealed the effects of independent variable son studies response parameters. Particle size increased with higher phospholipid choline and cholesterol concentrations (Fig. 2a and b), particularly at lower stirring speeds. However, at high stirring speeds (Fig. 2c), particle size followed a U-shaped pattern, with the smallest particles observed at moderate cholesterol levels. Entrapment efficiency improved consistently with increasing phospholipid choline

Table 2: ANOVA results for studied responses

Source	Y1			Y2			Y3		
	Sum of Squares	F-value	p-value	Sum of squares	F-value	p-value	Sum of squares	F-value	p-value
Model	32506.33	42.30	<0.0001*	559.55	61.43	<0.0001*	10.36	26.31	<0.0001*
A-Conc. of phosphatidyl choline	27191.12	283.05	<0.0001	392.28	387.60	<0.0001	0.0128	0.1951	0.6681
B-Conc. of Cholesterol	432.18	4.50	0.0667	2.76	2.73	0.1426	0.0618	0.9414	0.3548
C-stirring speed	477.41	4.97	0.0564	0.0050	0.0049	0.9459	0.1439	2.19	0.1694
AB	759.00	7.90	0.0228	10.60	10.47				
AC	10.56	0.1100	0.7487	8.32	8.22				
BC	460.10	4.79	0.0601	0.5852	0.5782				
A^2				57.29	56.61	0.0143	3.15	47.98	< 0.0001
B^2	2372.63	24.70	0.0011	41.28	40.79	0.0241	2.74	41.73	< 0.0001
C^2	655.01	6.82	0.0311	50.08	49.48	0.4718	3.19	48.56	< 0.0001
Residual	768.51			7.08		0.0001	0.6562		
Lack of Fit	768.51			7.08		0.0004	0.6562		
Pure Error	0.0000			0.0000		0.0002	0.0000		
Cor Total	33274.84			566.63			11.01		

ANOVA: Analysis of variance. *indicate significant values

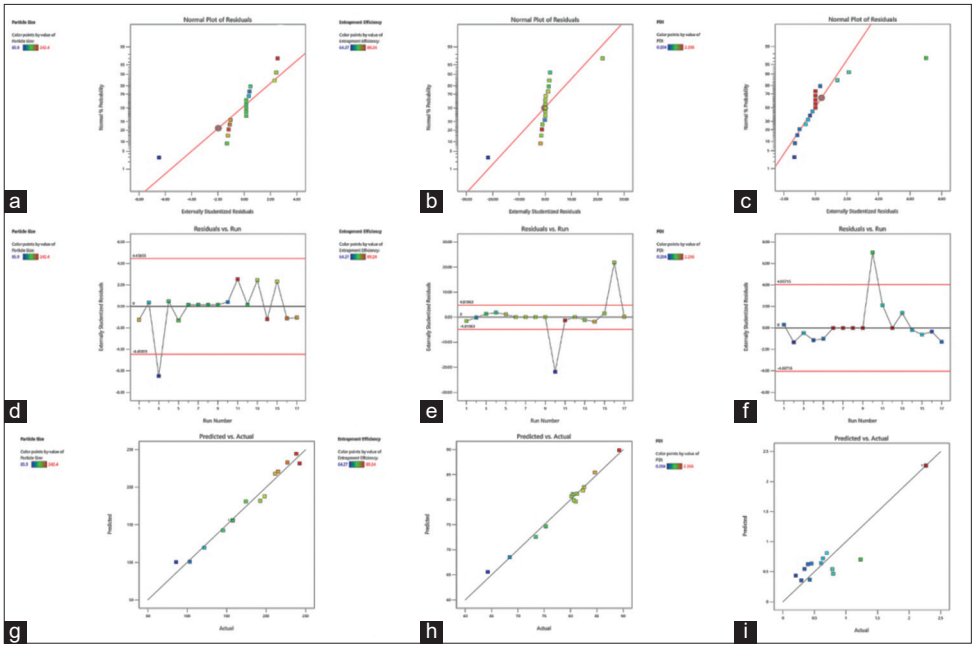

Fig. 1: Diagnostic plots for model validation of particle size, entrapment efficiency, and drug loading. (a-c) Normal probability plots of residuals; (d-f) Residuals versus run order plots showing randomness; (g-i) Predicted versus actual values confirming strong correlation and model accuracy

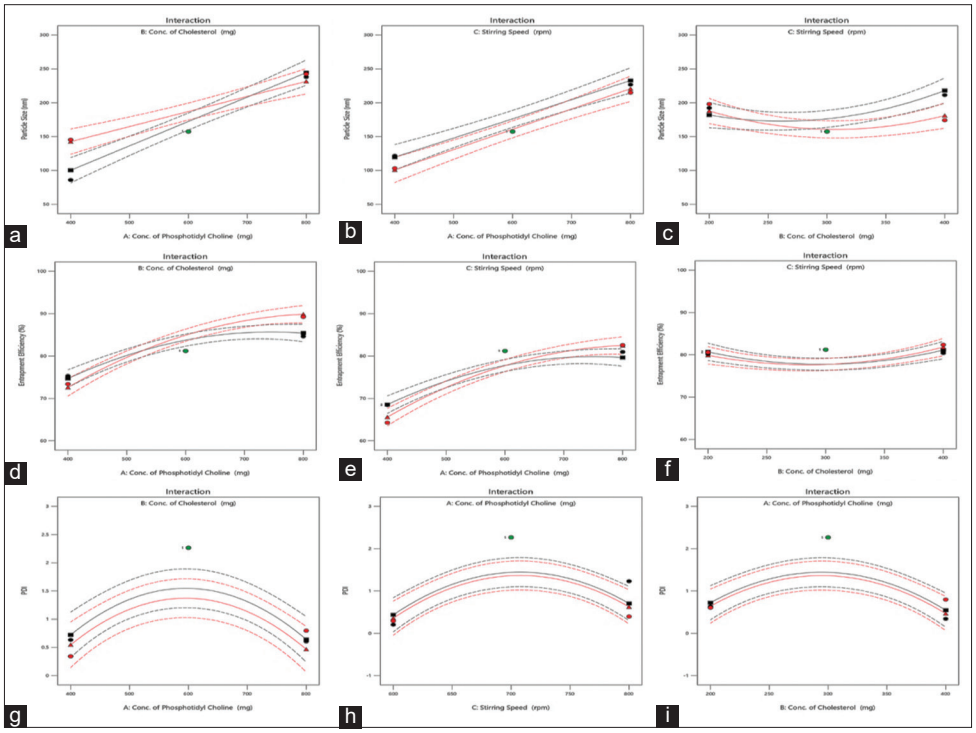

Fig. 2: Interaction plots illustrating the influence of formulation variables on particle size, entrapment efficiency, and polydispersity index (PDI). (a-c) Interaction effects on particle size; (d-f) Interaction effects on entrapment efficiency; (g-i) Interaction effects on PDI

and cholesterol concentrations (Fig. 2d and e). Higher stirring speeds (Fig. 2f) also enhanced efficiency, but the improvement was less pronounced at extreme levels of phospholipid choline. PDI exhibited a parabolic trend across all factors, indicating optimal uniformity at moderate levels of phospholipid choline, cholesterol concentration, and stirring speed (Fig. 2g-i). At higher levels of these factors, particle uniformity decreased. Overall, phospholipid choline concentration and stirring speed strongly influenced all responses, with cholesterol concentration playing a significant role in particle size and entrapment efficiency. Optimal conditions were achieved with moderate factor levels, balancing particle size, uniformity, and drug encapsulation.

The relation between variables and responses can be studied using the following equations,

$$Y1 = 156.04 + 58.30A + 7.35B - 7.73C - 13.77AB + 1.62AC - 10.73BC + 23.71B^2 + 12.46C^2$$

$$Y2 = 81.20 + 7.00A + 0.5875B - 0.0250C + 1.63AB + 1.44AC + 0.3825BC - 3.69A^2 + 3.13B^2 - 3.45C^2$$

$$Y3 = 2.27 - 0.0400A - 0.0879B + 0.1341C - 0.8648A^2 - 0.8065B^2 - 0.8700C^2$$

The 3D surface plots demonstrated the interactive effects of independent and dependent variables. In Fig. 3a, particle size increased with higher cholesterol and phospholipid choline concentrations. This trend could be attributed to the enhanced viscosity of the lipid matrix, which restricted shear forces during emulsification, leading to larger particles. Fig. 3b showed that while particle size increased with phospholipid choline concentration, higher stirring speeds reduced particle size by providing greater energy to break down lipid aggregates. In Fig. 3c, a U-shaped relationship between cholesterol and stirring speed suggested that moderate levels of both factors produced optimal particle sizes, likely due to a balance between lipid stabilization and sufficient energy for particle dispersion.

Fig. 3d demonstrated that entrapment efficiency improved with increased cholesterol and phospholipid choline concentrations. Cholesterol enhanced bilayer rigidity and reduced leakage, while higher phospholipid content provided more binding sites for the drug. In Fig. 3e, stirring speed facilitated better incorporation of the drug into the lipid matrix by promoting uniform dispersion, while higher phospholipid choline further stabilized the vesicles. Fig. 3f showed that cholesterol played a critical role, as higher concentrations increased drug encapsulation by stabilizing the lipid bilayer, but extremely high stirring speeds disrupted vesicle integrity, reducing efficiency.

3g and 3h revealed that PDI followed a parabolic trend, with lower PDI values (indicating better uniformity) achieved at moderate phospholipid choline and cholesterol concentrations. This likely resulted from optimal lipid alignment and reduced coalescence. Stirring speed also affected PDI, as moderate levels provided adequate energy for uniform particle distribution without causing destabilization. Fig. 3i confirmed that extreme levels of cholesterol or phospholipid choline introduced heterogeneity due to either excess rigidity or uneven particle breakup. These findings indicated that balanced levels of phospholipid choline, cholesterol, and stirring speed were crucial for achieving small particle size, high entrapment efficiency, and low PDI. Cholesterol enhanced structural stability, while stirring speed controlled particle dispersion, emphasizing the need for precise optimization of formulation variables.

Perturbation analysis (Fig. 4) showed that Factor A significantly increased particle size with larger deviations, while Factors B and C had minimal effects (Fig. 4a). Factor B positively influenced entrapment efficiency, whereas Factor A negatively impacted it, and Factor C showed negligible effects (Fig. 4b). The PDI displayed a bell-shaped trend, with optimal uniformity near the reference point (Fig. 4c). These findings highlighted Factor A's critical role in particle size, Factor B's importance in entrapment efficiency, and the combined influence of all factors on PDI optimization.

Model validation

The particle size of 120.52 nm, entrapment efficiency of 75.84%, PDI of 0.298, and overall desirability of 0.660 were expected to be produced by the optimized formulation, which was obtained at a phosphatidylcholine concentration of 436.35 mg, cholesterol concentration of 200 mg, and stirring speed of 617.50 rpm. The PDI of 0.294, entrapment efficiency of 77.23%, and particle size of 121.6 nm obtained from the experimental validation under these circumstances were all in good agreement with the expected values, confirming the suitability and dependability of the created model.

Characterization of formulation

Particle size and zeta potential

In comparison to the fresh formulation, the reconstituted freeze-dried sample's particle size was found to be larger, measuring 145.3 nm (Fig. 5a). However, the size obtained is deemed appropriate for enhanced absorption and stays within the acceptable nanometric range. Zeta potential was found to be −6.2 mV (Fig. 5b). Zeta potential was found to be lower. This could be attributed to interaction of Ca^{2+} with phospholipids. Similar findings were observed in the case of Curcumin NCs which showed zeta potential with a lower magnitude (−8.20 mV) than nanoliposomes [37].

FTIR study

The FTIR spectrum of pure diosmin (Fig. 6a) showed distinct peaks corresponding to its functional groups, confirming its structural identity. The broad peak at 3585 cm^{-1} was attributed to O-H stretching, characteristic of hydroxyl groups present in flavonoid compounds. Aliphatic C-H stretching was represented by the peak at 2856 cm^{-1}, whereas aromatic C-H stretching was indicated by a strong peak at 3060 cm^{-1}. The carbonyl group's C=O stretching was attributed to the

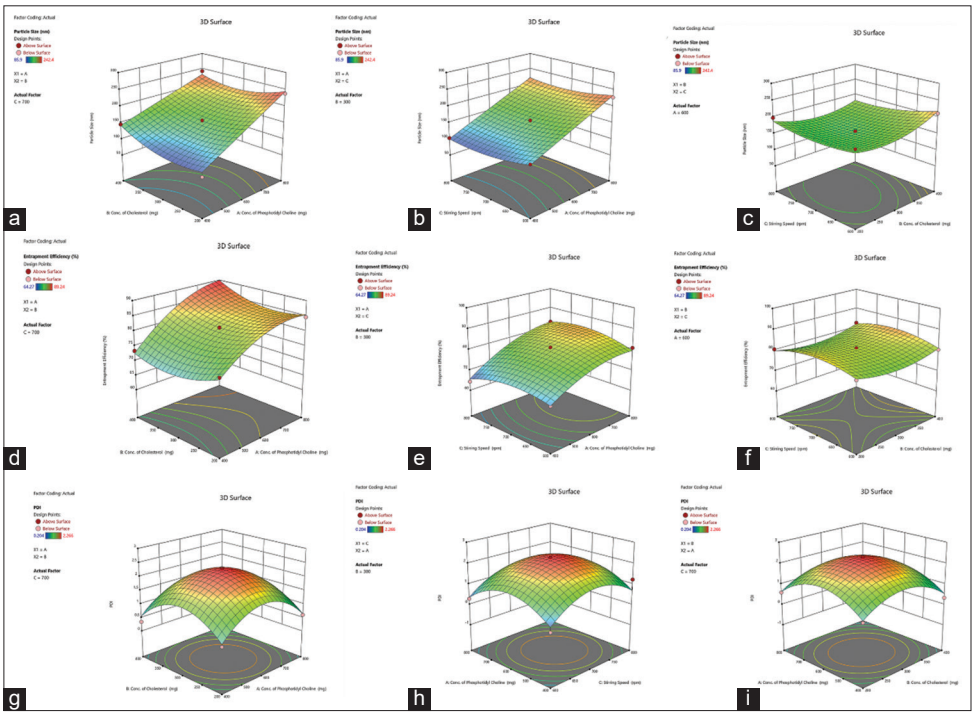

Fig. 3: 3D surface plots depicting the interaction effects of formulation. (a-c) 3D plots for particle size; (d-f) 3D plots for entrapment efficiency; (g-i) 3D plots for PDI

strong peak at 1653 cm^{-1}, whereas the ether group's C-O-C stretching was represented by the peak at 1259 cm^{-1}. Aromatic C-H bending vibrations were linked to peaks at 874 cm^{-1} and 980 cm^{-1}, which further supported the existence of functional groups unique to diosmin. These results validated Diosmin's identity and purity.

In the physical mixture containing diosmin, phosphatidylcholine, and cholesterol (Fig. 6b), the characteristic peaks of diosmin, such as O-H stretching at 3585 cm^{-1}, C=O stretching at 1653 cm^{-1}, and C-O-C stretching at 1259 cm^{-1}, were retained, suggesting that the structural integrity of diosmin remained intact. Additional peaks appeared at 2920 cm^{-1} and 1732 cm^{-1}, corresponding to the C-H stretching and ester C=O stretching of phosphatidylcholine and cholesterol, respectively. The O-H stretching peak at 3585 cm^{-1} displayed slight broadening, which indicated potential hydrogen bonding interactions between diosmin and the lipids. The absence of significant peak shifts suggested that the components were physically mixed without chemical interaction.

In the NC formulation of diosmin (Fig. 6c), several spectral changes were observed. The O-H stretching peak at 3585 cm^{-1} showed a significant reduction in intensity, indicating strong interactions between diosmin and the lipid bilayers. In addition, the C=O stretching peak of diosmin, originally observed at 1653 cm^{-1}, shifted to a lower wavenumber (~1630 cm^{-1}), which suggested encapsulation and hydrogen bonding with phosphatidylcholine and cholesterol. Peaks corresponding to the lipids, such as the ester C=O stretching at 1732 cm^{-1}, exhibited reduced intensity, further supporting their involvement in forming the NC structure. The retention of aromatic C-H bending vibrations at 874 cm^{-1} and 980 cm^{-1} confirmed that diosmin remained intact within the formulation.

These spectral changes, particularly the reduction in intensity and the shift of O-H and C=O stretching peaks, demonstrated the successful encapsulation of diosmin within the lipid bilayers. The interactions between diosmin and the lipids, along with the absence of separate diosmin peaks, confirmed the formation of NCs. This encapsulation is expected to enhance the stability and bioavailability of diosmin in the formulation.

DSC analysis

The DSC thermogram of pure diosmin (Fig. 7a) displayed a sharp endothermic peak at approximately 118.71°C, corresponding to its melting point, indicating its crystalline nature. This was further evidenced by the sharpness of the peak, which suggested high purity and well-defined crystalline structure. A significant weight loss observed around this temperature aligned with the thermal decomposition of diosmin.

In contrast, the thermogram of D-NC (Fig. 7b) exhibited a broader and shifted endothermic peak at 112.35°C. The decrease in peak intensity and a slight shift in the melting point suggested a reduction in crystallinity due to the encapsulation of diosmin within the NC matrix.

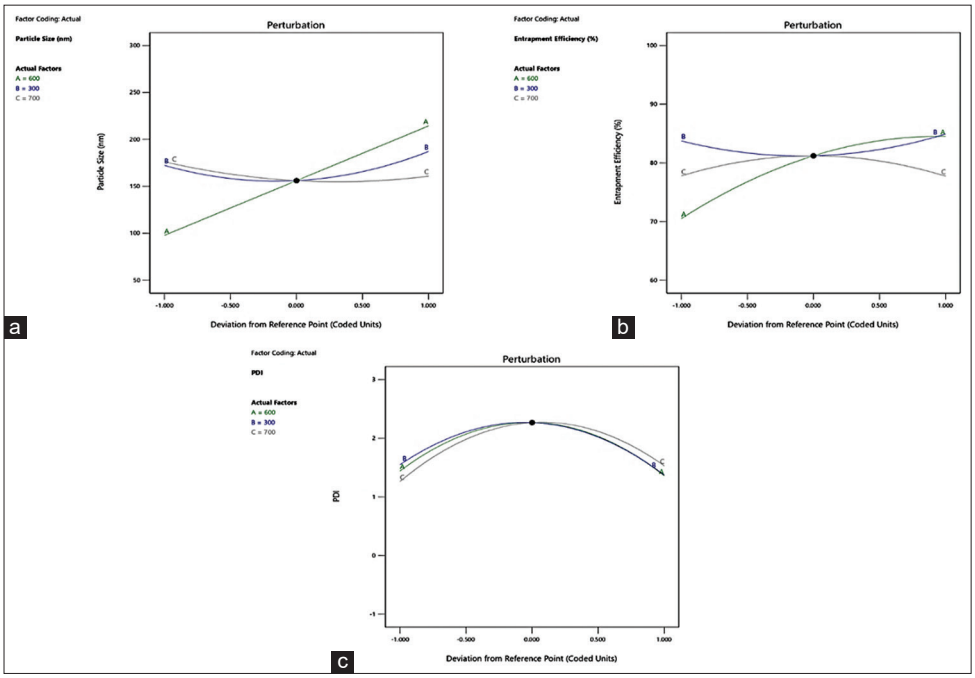

Fig. 4: Perturbation plots illustrating the individual effects of formulation variables on (a) particle size, (b) entrapment efficiency, and (c) polydispersity index

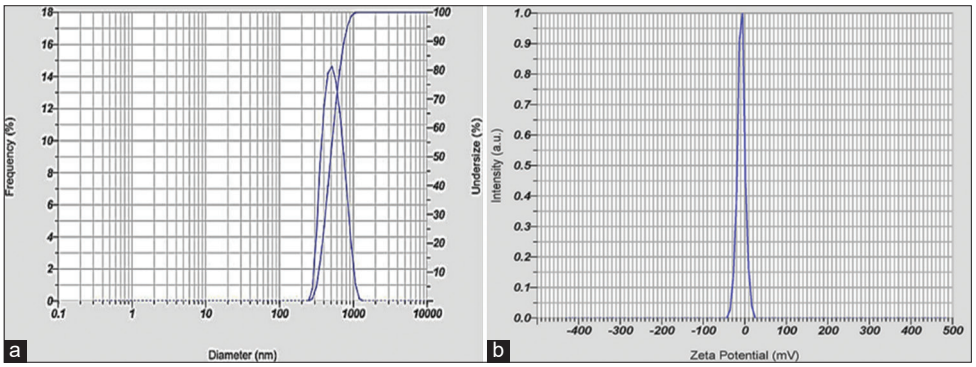

Fig. 5: (a and b) Particle size and zeta potential of optimized formulation

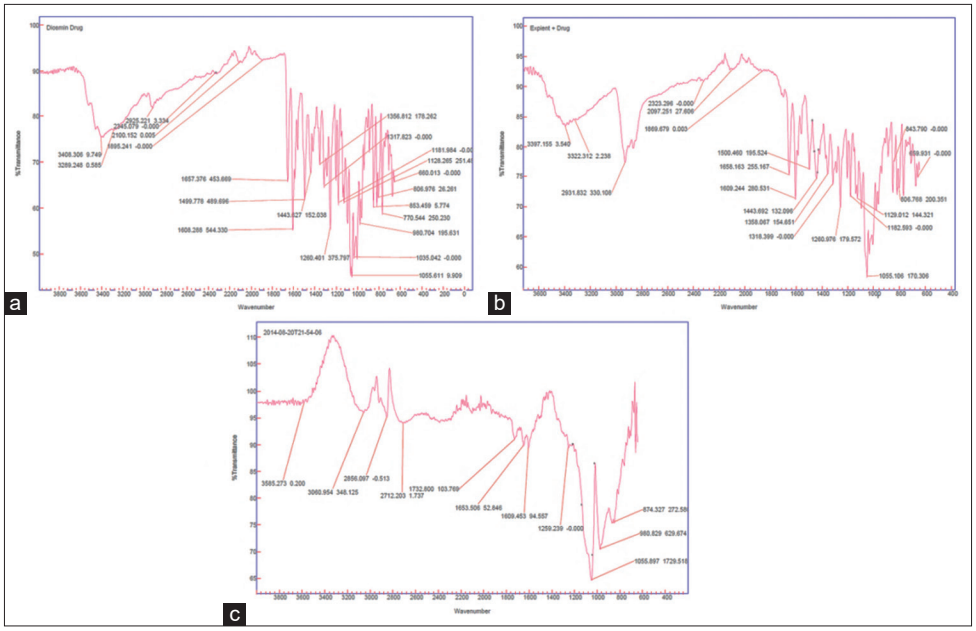

Fig. 6: Fourier-transform infrared spectroscopy spectrum of (a) Pure drug, (b) Physical mixture, and (c) Formulation

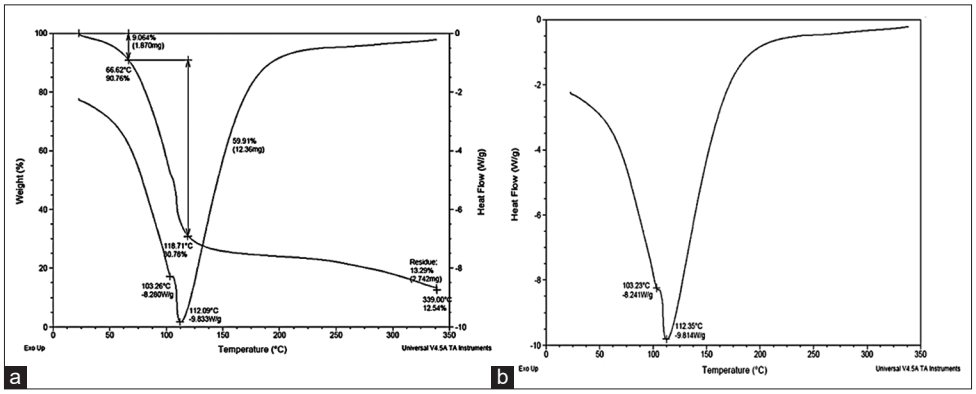

Fig. 7: Differential scanning calorimetry thermogram of (a) pure drug and (b) formulation

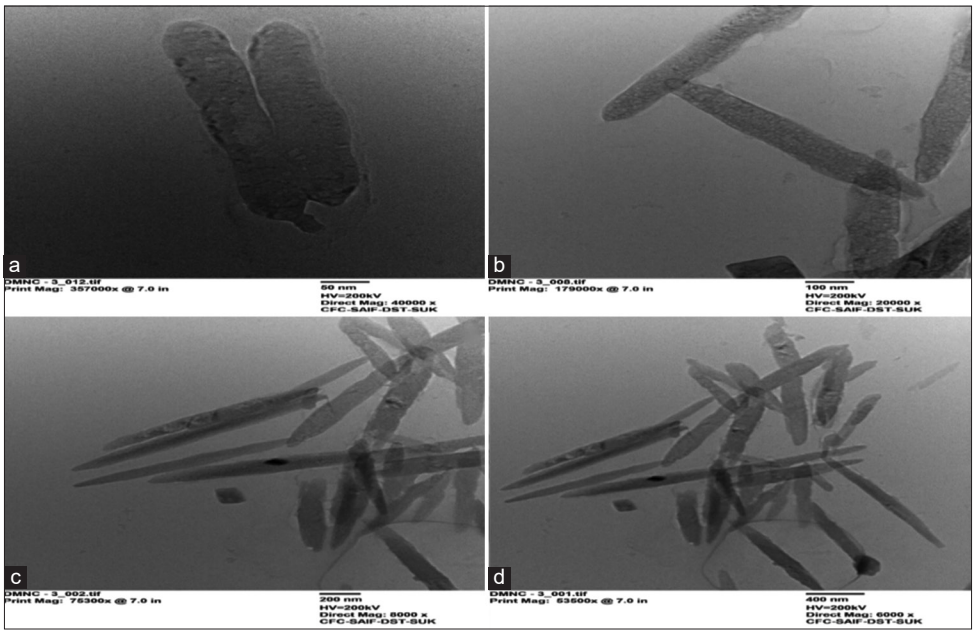

Fig. 8: (a-d) Transmission electron microscopy images of nanocochleates

This thermal behavior indicated successful entrapment of diosmin, which was likely dispersed in an amorphous or less crystalline state within the lipid-based system. The lack of additional peaks in the NC thermogram confirmed the absence of physical interactions or unencapsulated diosmin, signifying effective formulation.

TEM analysis

The TEM images (Fig. 8a-d) confirm the successful formation of NCs, exhibiting characteristic cylindrical and rod-like morphologies. Fig. 8a shows tightly packed, multilamellar structures at high magnification, while Fig. 8b reveals elongated, rolled-up lipid bilayers typical of cochleates. Fig. 8c and d display a uniform distribution of these structures at lower magnifications, with sizes ranging from 200 to 400 nm. The observed multilayered architecture confirms the stable and organized nature of the NCs, suitable for drug encapsulation and controlled release.

***In vitro* dissolution study**

The *in vitro* dissolution profiles of the pure drug (Diosmin) and the optimized D-NC formulation were evaluated over a period of 24 h. The dissolution data reveal a distinct difference in the drug release rates between the two samples. For the pure drug, the release was gradual, reaching 14.26% at 2 h, 22.64% at 4 h, 28.69% at 6 h, and progressively increasing to a maximum of 47.05% at 24 h. This relatively slow dissolution rate suggests limited solubility and potential dissolution challenges of the pure drug in its native form, consistent with Diosmin's hydrophobic nature. In contrast, the optimized NC formulation showed a significantly enhanced dissolution rate, with 34.45% release observed at 2 min, followed by 57.78% at 4 h, and a rapid increase to 95.62% at 24 h. These results indicate that the NCs improved the dissolution rate of Diosmin, achieving almost complete release within the 24- h timeframe (Fig. 9).

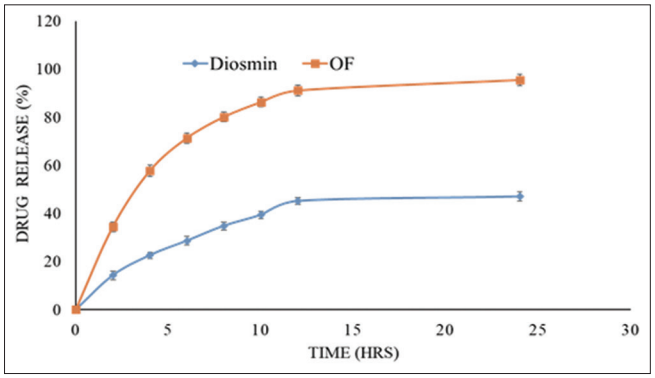

Fig. 9: *In vitro* dissolution profiles of pure drug and optimized formulation

The observed enhancement in dissolution for the NC formulation can be attributed to the nanoscale structure and encapsulation properties of the NCs. NCs offer a high surface area-to-volume ratio, which improves the solubility and dissolution rate of hydrophobic drugs like Diosmin by reducing particle size and enhancing drug dispersion in the dissolution medium. In addition, the lipid bilayer structure of NCs may facilitate better wetting of the drug particles, further promoting dissolution. The rapid and nearly complete dissolution profile of the D-NC suggests its potential for improved bioavailability of Diosmin when compared to the pure drug.

Cell cycle analysis

The cell cycle distribution of MCF-7 cells treated with the formulation was analyzed using flow cytometry to assess the anticancer efficacy of the test formulation. In the untreated control (Fig. 10a and c), the distribution was as follows: 1.08% of cells in the SubG1 phase, 44.6% in the G1/G0 phase, 13.8% in the S phase, and 37.8% in the G2/M phase. These values reflect the normal cell cycle distribution of MCF-7 cells, with the majority of cells in the G1/G0 and G2/M phases, and minimal apoptosis (SubG1 phase) observed. In contrast, the drug-treated sample (Fig. 10b and c) displayed significant shifts in cell cycle distribution, indicative of the formulation's anticancer effects. A significant increase in apoptosis in response to therapy was indicated by the SubG1 population, which rose to 29%. A decrease in DNA synthesis and cell proliferation was shown by the G1/G0 phase dropping to 27.9% and the S phase dropping to 11.9%. In addition, the G2/M phase dropped to 23.5%, indicating a slower rate of cell division.

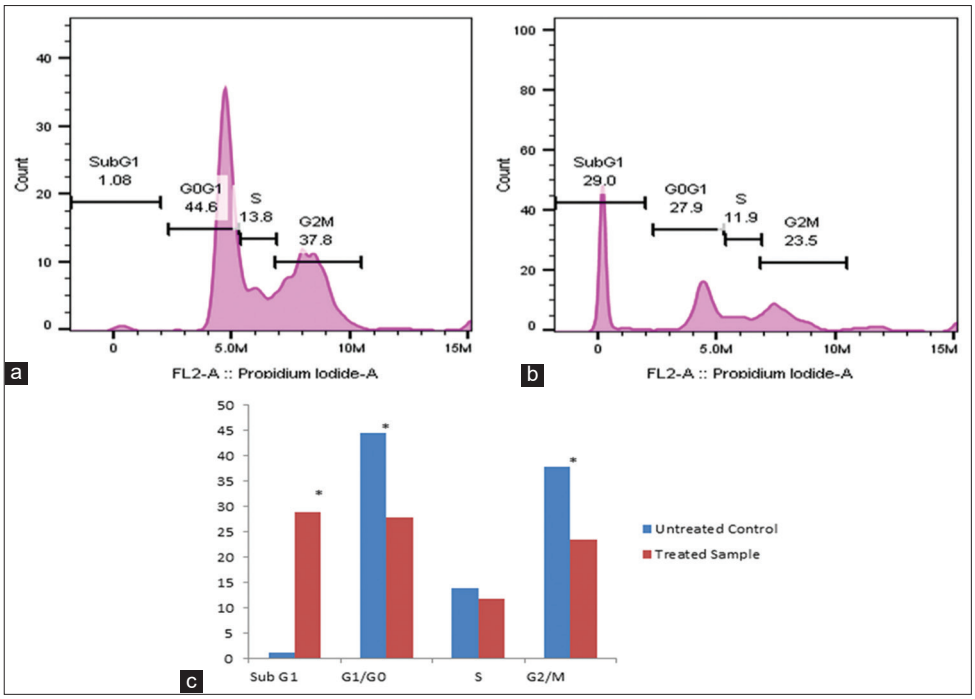

Fig. 10: Cell cycle analysis of (a) untreated cells and (b) formulation treated cells. (c) Represent graphical representation of percentage of cells in each phase of cell cycle. *indicate significant difference ($p<0.05$) between treated and untreated cells

The substantial increase in the SubG1 population and the reduction in G1/G0, S, and G2/M populations collectively demonstrate the efficacy of the formulation in inducing cell cycle arrest and promoting apoptosis in MCF-7 cells. These alterations suggest that the test formulation disrupts normal cell cycle progression, effectively inhibiting cell proliferation and inducing cell death, which are desirable outcomes in anticancer treatment. Given the considerable rise in apoptotic markers and disruption of cell cycle phases required for cancer cell proliferation, the data clearly indicate this formulation's potential as an anticancer agent against breast cancer cells. Results are akin to other CDK6 inhibitors [55].

CONCLUSION

This study successfully developed and optimized D-NCs as a targeted delivery system for cancer therapy. The BBD revealed the significant impact of phospholipid choline, cholesterol, and stirring speed on critical formulation characteristics such as particle size, entrapment efficiency, and PDI. The robust model, supported by diagnostic plots and strong predictive accuracy, highlighted the favorable formulation parameters. FTIR and DSC analyses confirmed the effective encapsulation of diosmin, while in vitro release studies demonstrated sustained drug release, enhancing its solubility and availability. Furthermore, cell cycle analysis in MCF-7 breast cancer cells provided evidence of the formulation's antiproliferative activity. Overall, the optimized D-NCs present a promising approach in cancer nanomedicine, offering improved encapsulation, stability, controlled release, and therapeutic potential for targeted treatment.

AUTHOR'S CONTRIBUTION

Sardar Shelake and Shitalkumar Patil designed the formulation using Design of Experiment and analytical characterization. Structured and edited the manuscript and also provided conceptualization, overall supervision of the research work, ensured methodological validation, critically revised the manuscript, and approved the final version for submission. Both authors have read and approved the final version of the manuscript.

CONFLICTS OF INTEREST

No conflicts of interest.

AUTHOR'S FUNDING

The authors declare that the present research was conducted without any financial assistance from government, commercial, or non-profit funding agencies.

REFERENCES

1. Bhagwat DA, Swami PA, Nadaf SJ, Choudhari PB, Kumbar VM, More HN, *et al*. Capsaicin loaded solid SNEDDS for enhanced bioavailability and anticancer activity: *In-vitro, in-silico*, and *in-vivo* characterization. J Pharm Sci. 2021;110(1):280-91. doi: 10.1016/j.xphs.2020.10.020, PMID 33069713
2. Kumbar VM, Muddapur U, Bin Muhsinah A, Alshehri SA, Alshahrani MM, Almazni IA, *et al*. Curcumin-encapsulated nanomicelles improve cellular uptake and cytotoxicity in cisplatin-resistant human oral cancer cells. J Funct Biomater. 2022;13(4):158. doi: 10.3390/jfb13040158, PMID 36278627
3. Arnold M, Morgan E, Rumgay H, Mafra A, Singh D, Laversanne M, *et al.* Current and future burden of breast cancer: Global statistics for 2020 and 2040. Breast. 2022 Dec;66:15-23. doi: 10.1016/j.breast.2022.08.010. PMID 36084384
4. Kumbhar P, Kole K, Khadake V, Marale P, Manjappa A, Nadaf S, *et al*. Nanoparticulate drugs and vaccines: Breakthroughs and bottlenecks of repurposing in breast cancer. J Control Release. 2022 Sep;349:812-30. doi: 10.1016/j.jconrel.2022.07.039, PMID 35914614
5. Mehdi S, Chauhan A, Dhutty A. Cancer and new prospective to treat cancer. Int J Curr Pharm Res. 2023;15(6):16-22. doi: 10.22159/ijcpr.2023v15i6.3078
6. Randive DS, Shejawal KP, Bhinge SD, Bhutkar MA, Jadhav NR, Patil SB, *et al*. Efficient *in vitro* oxaliplatin delivery with functionalized single-walled carbon nanotube for enhanced colon cancer treatment. Futur J Pharm Sci. 2023;9(1):91. doi: 10.1186/s43094-023-00543-8
7. Kumbhar P, Khade V, Khadake V, Marale P, Manjappa A, Nadaf S, *et al*. Ifosfamide-loaded cubosomes: An approach to potentiate cytotoxicity against MDA-MB-231 breast cancer cells. Fabad J Pharm Sci. 2022;48(1):37-52. doi: 10.55262/fabadeczacilik.1145208
8. Gerges SH, Wahdan SA, Elsherbiny DA, El-Demerdash E. Pharmacology of diosmin, a citrus flavone glycoside: An updated review. Eur J Drug Metab Pharmacokinet. 2022 Jan;47(1):1-18. doi: 10.1007/s13318-021-00731-y, PMID 34687440
9. Rahman L, Talha Khalil A, Ahsan Shahid S, Shinwari ZK, Almarhoon ZM, Alalmaie A, *et al*. Diosmin: A promising phytochemical for functional foods, nutraceuticals and cancer therapy. Food Sci Nutr. 2024;12(9):6070-92. doi: 10.1002/fsn3.4271, PMID 39554345
10. Kakkos SK, Nicolaides AN. Efficacy of micronized purified flavonoid fraction (Daflon®) on improving individual symptoms, signs and quality of life in patients with chronic venous disease: A systematic review and meta-analysis of randomized double-blind placebo-controlled trials. Int Angiol. 2018;37(2):143-54. doi: 10.23736/S0392-9590.18.03975-5, PMID 29385792
11. Sheikh P, Lohsiriwat V, Shelygin Y. Micronized purified flavonoid fraction in hemorrhoid disease: A systematic review and meta-analysis. Adv Ther. 2020;37(6):2792-812. doi: 10.1007/s12325-020-01353-7, PMID 32399811
12. Rajasekar M, Baskaran P, Mary J, Sivakumar M, Selvam M. Revisiting diosmin for their potential biological properties and applications. Carbohydr Polym Technol Appl. 2024;7:100419. doi: 10.1016/j.carpta.2023.100419
13. Huwait E, Mobashir M. Potential and therapeutic roles of diosmin in human diseases. Biomedicines. 2022;10(5):1076. doi: 10.3390/biomedicines10051076, PMID 35625813
14. Ma C, Dan M, Wang Y, Shu C, Jiao M, Shao Y, *et al.* Diosmin reduces the stability of Snail and cyclin D1 by targeting FAK to inhibit NSCLC progression. Phytomedicine. 2024;135:156135. doi: 10.1016/j.phymed.2024.156135, PMID 39405613
15. Chang YL, Li YF, Chou CH, Huang LC, Wu YP, Kao Y, *et al*. Diosmin inhibits glioblastoma growth through inhibition of autophagic flux. Int J Mol Sci. 2021;22(19):10453. doi: 10.3390/ijms221910453, PMID 34638796
16. Musyayyadah H, Wulandari F, Nangimi AF, Anggraeni AD, Ikawati M, Meiyanto E. The growth suppression activity of diosmin and PGV-1 co-treatment on 4T1 breast cancer targets mitotic regulatory proteins. Asian Pac J Cancer Prev. 2021;22(9):2929-38. doi: 10.31557/APJCP.2021.22.9.2929, PMID 34582664
17. Anwer MK, Shakeel F. Measurement and correlation of solubility of diosmin in four pure solvents and β-cyclodextrin solution at 298.15K to 333.15K. Chin J Chem Eng. 2015;23(5):812-5. doi: 10.1016/j.cjche.2014.03.006
18. Freag MS, Elnaggar YS, Abdallah OY. Development of novel polymer-stabilized diosmin nano suspensions*: In vitro* appraisal and *ex vivo* permeation. Int J Pharm. 2013;454(1):462-71. doi: 10.1016/j.ijpharm.2013.06.039, PMID 23830765
19. Zheng Y, Zhang R, Shi W, Li L, Liu H, Chen Z, *et al.* Metabolism and pharmacological activities of the natural health-benefiting compound diosmin. Food Funct. 2020 Oct 21;11(10):8472-92. doi: 10.1039/d0fo01598a, PMID 32966476
20. Mustafa S, Akbar M, Khan MA, Sunita K, Parveen S, Pawar JS, *et al.* Plant metabolite diosmin as the therapeutic agent in human diseases. Curr Res Pharmacol Drug Discov. 2022;3:100122. doi: 10.1016/j.crphar.2022.100122, PMID 36568270
21. Xie L, Cai C, Cao Y, Li X. Tea saponins as novel stabilizers for the development of diosmin nanosuspensions: Optimization and *in vitro* evaluation. J Drug Deliv Sci Technol. 2023;90:105118. doi: 10.1016/j.jddst.2023.105118
22. Sun WX, Zhang CT, Yu XN, Guo JB, Ma H, Liu K, *et al*. Preparation and pharmacokinetic study of diosmetin long-circulating liposomes modified with lactoferrin. J Funct Foods. 2022;91:105027. doi: 10.1016/j.jff.2022.105027
23. Rahman M, Almalki WH, Afzal O, Kazmi I, Alfawaz Altamimi AS, Alghamdi S, *et al.* Diosmin-loaded solid nanoparticles as nano-antioxidant therapy for management of hepatocellular carcinoma: QbD-based optimization, *in vitro* and *in vivo* evaluation. J Drug Deliv Sci Technol. 2021;61:102213. doi: 10.1016/j.jddst.2020.102213
24. Li S, Guan T, Lv H, Cai Y, Cao W, Zhang Z, *et al*. Fabrication of diosmin-loaded food-grade bilayer nanoparticles with modified chitosan and soy peptides and antioxidant properties examination. Food Chem X. 2024;21:101237. doi: 10.1016/j.fochx.2024.101237, PMID 38426075

25. Sahu N, Soni D, Chandrashekhar B, Satpute DB, Saravanadevi S, Sarangi BK, *et al.* Synthesis of silver nanoparticles using flavonoids: Hesperidin, naringin and diosmin, and their antibacterial effects and cytotoxicity. Int Nano Lett. 2016;6(3):173-81. doi: 10.1007/s40089-016-0184-9
26. Zingale E, Rizzo S, Bonaccorso A, Consoli V, Vanella L, Musumeci T, *et al*. Optimization of lipid nanoparticles by response surface methodology to improve the ocular delivery of diosmin: Characterization and *in-vitro* anti-inflammatory assessment. Pharmaceutics. 2022;14(9):1961. doi: 10.3390/pharmaceutics14091961, PMID 36145708
27. Anwer MK, Ahmed MM, Aldawsari MF, Iqbal M, Kumar V. Preparation and evaluation of diosmin-loaded diphenyl carbonate-cross-linked Cyclodextrin Nanosponges for breast cancer therapy. Pharmaceuticals (Basel). 2022;16(1):19. doi: 10.3390/ph16010019, PMID 36678517
28. Anwer MK, Jamil S, Ansari MJ, Al-Shdefat R, Ali BE, Ganaie MA, *et al*. Water soluble binary and ternary complexes of diosmin with β-cyclodextrin: Spectroscopic characterization, release studies and anti-oxidant activity. J Mol Liq. 2014;199:35-41. doi: 10.1016/j.molliq.2014.08.012
29. Tilawat M, Bonde S. Nanocochleates: A potential drug delivery system. J Mol Liq. 2021;334:116115. doi: 10.1016/j.molliq.2021.116115
30. Verekar R, Dessai S, Ayyanar M, Nadaf S, Gurav S. Nanocochleates: Revolutionizing lipid-based drug delivery with enhanced bioavailability, a review. Hybrid Adv. 2024;6:100215. doi: 10.1016/j.hybadv.2024.100215
31. Hajare AA, Mali SS, Ahir AA, Thorat JD, Salunkhe SS, Nadaf SJ, *et al*. Lipid nanoparticles: A modern formulation approach in topical drug delivery systems. J Adv Drug Deliv. 2014;1(1):30-7.
32. Nadaf S, Killedar S. Development and validation of RP–HPLC method for estimation of curcumin from nanocochleates and its application in *in-vivo* pharmacokinetic study. Acta Chim Slov. 2020;67:1100-10. doi: 10.17344/acsi.2020.5892
33. Shelake S, Ingrole A, Chougule N. Preparation optimization and evaluation of lenvatinib as a nanocochleate. Int J Pharm Sci. 2024;2(7):2136-42. doi: 10.5281/zenodo.13131860
34. Nadaf S, Killedar S. Novel liposome derived nanoparticulate drug delivery system. Cre J Pha Res 2015.1;3:117-28.
35. Panda P, De M, Basak S. Nanocochleates. In: Ray S, Nayak AK, editors. Design and Applications of Theranostic Nanomedicines. New Delhi: Woodhead Publishing; 2023. p. 143-73. doi: 10.1016/B978-0-323-89953-6.00006-4
36. Bothiraja C, Rajput N, Poudel I, Rajalakshmi S, Panda B, Pawar A. Development of novel biofunctionalized chitosan decorated nanocochleates as a cancer targeted drug delivery platform. Artif Cells Nanomed Biotechnol. 2018;46(Sup1):447-61. doi: 10.1080/21691401.2018.1430584, PMID 29368543
37. Nadaf SJ, Killedar SG. Curcumin nanocochleates: Use of design of experiments, solid state characterization, *in vitro* apoptosis and cytotoxicity against breast cancer MCF-7 cells. J Drug Deliv Sci Technol. 2018;47:337-50. doi: 10.1016/j.jddst.2018.06.026
38. Hossain S, Islam A, Tasnim F, Hossen F, E-Zahan K, Asraf A. Antimicrobial, antioxidant and cytotoxicity study of Cu(II), Zn(II), Ni(II), and Zr(IV) complexes containing O, N donor Schiff base ligand. Int J Chem Res. 2024;8(4):1-11. doi: 10.22159/ijcr.2024v8i4.231
39. Jadhav S, Yadav A, Nadaf S. Enhanced antidiabetic performance through optimized charantin-loaded nanostructured lipid carriers: Formulation and *in vivo* studies in diabetic mice. J Drug Deliv Sci Technol. 2024;101(A):106208. doi: 10.1016/j.jddst.2024.106208
40. Andrade F, Jenipher C, Gurav N, Nadaf S, Khan MS, Kalaskar M, *et al*. Endophytic fungus *Colletotrichum siamense* derived silver nanoparticles: Biomimetic synthesis, process optimization and their biomedical applications. J Inorg Organomet Polym. 2024;34(12):6056-70. doi: 10.1007/s10904-024-03235-9
41. Mane V, Killedar S, More H, Nadaf S, Salunkhe S, Tare H. Novel phytosomal formulation of *Emblica officinalis* extracts with its *in vivo* nootropic potential in rats: Optimization and development by Box-Behnken design. J Chem. 2024;2024:6644815. doi: 10.1155/2024/6644815
42. Dhavale RP, Nadaf SJ, Bhatia MS. Quantitative structure property relationship assisted development of fluocinolone acetonide loaded transfersomes for targeted delivery. J Drug Deliv Sci Technol. 2021;65:102758. doi: 10.1016/j.jddst.2021.102758
43. Gracias S, Ayyanar M, Peramaiyan G, Kalaskar M, Redasani V, Gurav N, *et al*. Fabrication of chitosan nanocomposites loaded with biosynthetic metallic nanoparticles and their therapeutic investigation. Environ Res. 2023;234:116609. doi: 10.1016/j.envres.2023.116609, PMID 37437861
44. Kumbhar PS, Manjappa AS, Shah RR, Nadaf SJ, Disouza JI. Nanostructured lipid carrier-based gel for repurposing simvastatin in localized treatment of breast cancer: Formulation design, development, and *in vitro* and *in vivo* characterization. AAPS PharmSciTech. 2023;24(5):106. doi: 10.1208/s12249-023-02565-0, PMID 37085596
45. Nadaf S, Jena GK, Rarokar N, Gurav N, Ayyanar M, Prasad S, *et al*. Biogenic and biomimetic functionalized magnetic nanosystem: Synthesis, properties, and biomedical applications. Hybrid Adv. 2023;3:100038. doi: 10.1016/j.hybadv.2023.100038
46. Kumbhar P, Waghmare P, Nadaf S, Manjappa A, Shah R, Disouza J. QbD and Six Sigma quality approach for chromatographic estimation of repurposed simvastatin from nanostructured lipid carriers. Microchem J. 2023;185:108310. doi: 10.1016/j.microc.2022.108310
47. Usapkar P, Saoji S, Jagtap P, Ayyanar M, Kalaskar M, Gurav N, *et al*. QbD-guided phospholipid-tagged nanonized boswellic acid naturosomal delivery for effective rheumatoid arthritis treatment. Int J Pharm X. 2024;7:100257. doi: 10.1016/j.ijpx.2024.100257, PMID 39668885
48. Rudroju A, Mothilal M. Development of nano sponges-based topical formulation for the effective delivery of selected antifungal drug. Int J Appl Pharm. 2024;16(5):146-55.
49. Nadaf SJ, Killedar SG, Kumbar VM, Bhagwat DA, Gurav SS. Pazopanib-laden lipid based nanovesicular delivery with augmented oral bioavailability and therapeutic efficacy against non-small cell lung cancer. Int J Pharm. 2022;628:122287. doi: 10.1016/j.ijpharm.2022.122287, PMID 36257467
50. Jadhav NR, Kambar RS, Nadaf SJ, Phadatare PD. Design, development, *in vitro* and *in vivo* evaluation of multicomponent tablet formulation for enteral delivery of atorvastatin calcium and felodipine. J Pharm Investig. 2015;45(2):115-30. doi: 10.1007/s40005-014-0148-x
51. Al Hattali WS, Samuel BA, Philip AK. Enhancing fluconazole solubility and bioavailability through solid dispersion techniques: Evaluation of polyethylene glycol 6000 and sodium carboxymethyl cellulose systems using fiber optics. Int J Pharm Pharm Sci. 2024;16(12):51-9. doi: 10.22159/ijpps.2024v16i12.52739
52. Nadaf SJ, Savekar PL, Bhagwat DA, Dagade KV, Gurav SS. Revolutionizing fast disintegrating tablets: Harnessing a dual approach with porous starch and sublimation technique. Heliyon. 2024;10(19):e38793. doi: 10.1016/j.heliyon.2024.e38793, PMID 39430475
53. Savekar PL, Nadaf SJ, Killedar SG, Kumbar VM, Hoskeri JH, Bhagwat DA, *et al*. Citric acid cross-linked pomegranate peel extract-loaded pH-responsive β-cyclodextrin/carboxymethyl tapioca starch hydrogel film for diabetic wound healing. Int J Biol Macromol. 2024;274(1):133366. doi: 10.1016/j.ijbiomac.2024.133366, PMID 38914385
54. Tandale P, Suttee A, Panzade P, Gadade D. Quercetin-loaded graphene oxide nanoparticles: Synthesis, optimization, and evaluation for breast cancer treatment. Int J Appl Pharm. 2025;17(3):243-51.
55. Chukwuemeka PO, Umar HI, Iwaloye O, Oretade OM, Olowosoke CB, Oretade OJ, *et al*. Predictive hybrid paradigm for cytotoxic activity of 1,3,4-thiadiazole derivatives as CDK6 inhibitors against human (MCF-7) breast cancer cell line and its structural modifications: Rational for novel cancer therapeutics. J Biomol Struct Dyn. 2022;40(18):8518-37. doi: 10.1080/07391102.2021.1913231, PMID 33890551